Cover-zone protective qualities under corrosive environments

Cover-zone protective qualities under corrosive environments

Jaehwan Kim[1], W. John McCarter*[2], Benny Suryanto[2]

[1] Formerly School of Energy, Geoscience, Infrastructure and Society, now Korea Institute of Civil Engineering and Building Technology, 283, Goyang-daero, Ilsanseo-gu, Goyang-si, Gyeonggi-do, 10223, South Korea.

[2] School of Energy, Geoscience, Infrastructure and Society, Heriot-Watt University, Edinburgh, EH14 4AS, United Kingdom,

* Corresponding Author

E-mail: w.j.mccarter@hw.ac.uk

Tel: +44 (0)131 451 3318

ORCID:

William J McCarter: 0000-0002-1949-2856

Benny Suryanto: 0000-0002-3979-9994

ABSTRACT

The protective qualities of the concrete cover-zone and the condition of the embedded steel (active/passive) surface were studied using reinforced concrete slabs subjected to intermittent wetting/drying. The cementitious binders used within the experimental programme comprised plain Portland cement (CEM I) and Portland cement partially replaced with fly-ash (FA) and ground granulated blast-furnace slag (GGBS) with water/binder (w/b) ratios of 0.4 and 0.6. The concrete surface was exposed to a 0.55 Molar (3.2%) chloride solution with the intermittent regime extending over a period of ~400 days. Pairs of stainless steel electrodes were positioned within the cover-zone to monitor changes in electrical resistance/resistivity as chlorides migrated through the concrete, whereas macro-cell current and half-cell potential measurements were used to study corrosion initiation on the steel surface. In addition, at the end of the experimental programme, chloride profiling and gravimetric mass-loss measurements were obtained. For the analysis of electrical measurements, a *normalisation* method was employed to study chloride transport within the cover-zone. It was found that ongoing hydration (and resulting pore structure refinement) was the main factor for the increase in the bulk electrical resistance/resistivity of concrete and that chloride ingress was the main factor for the reduction in resistance/resistivity. The resistance/resistivity varied depending on the depth of the chloride penetration. It was shown that both binder type and w/b had a significant influence on the performance of the cover-zone and that the electrical properties of concrete could be developed as a candidate indicator of concrete performance.

Keywords: reinforced concrete, electrical resistivity, macro-cell current, half-cell potential, chloride-induced corrosion.

48 **Highlights**

49

50 • Discretized electrical measurements allow an integrated assessment of the cover

51 • A novel resistivity normalisation technique is introduced to study chloride ingress

52 • Ongoing hydration and pozzolanic reaction detected using electrical measurements

53

1. Introduction

Over the coming years, industrialised countries will be challenged to repair, maintain and expand their civil engineering infrastructure. The most widely used construction material is reinforced concrete and there is, more than ever, an increasing demand to reduce the overall environmental impact of this infrastructure together with a long service life (at least 100-years) and low/minimum maintenance. Regarding the long-term durability of reinforced concrete, chloride-induced corrosion of the embedded steel is the most commonly reported deterioration mechanism accounting for approximately 40% of reported cases [1]. Contamination of the concrete by chlorides mainly occurs through the use of de-icing salt used on roads for winter maintenance purposes or where concrete is placed near, or in, a marine environment.

According to Tuutti's model [2], deterioration caused by chloride attack in reinforced concrete structures comprises two components:

(i) an initiation period related to chloride transport through the concrete cover-zone and the build-up of chlorides at the steel surface to a certain critical level; and,

(ii) an active period related to the development of corrosion products on the steel surface and corrosion propagation.

Monitoring both these components of service-life is important in the study of the deterioration and performance of reinforced concrete structures. As it is the concrete cover-zone that protects the steel from the natural environment, this region of concrete is of considerable interest to engineers as the service-life of a structure depends, to a large extent, on the permeation properties of the concrete in this zone.

Chloride induced corrosion is a topic which has been given significant attention over recent years. Numerous studies have now been made in this regard which include, chloride penetration into concrete; the steel corrosion process; the development of testing techniques and corrosion

prevention and mitigation methods [see, for example, 3–13] leading to the development of both national and international specifications [14–18]. However, the influence of chloride ingress on concrete performance, in terms of its ability to protect the reinforcing steel, still remains a difficult task to assess due to numerous influencing factors including (but not limited to) variations in exposure conditions, initial condition of the steel and variations in concrete properties. To develop an efficient maintenance programme for reinforced concrete structures subjected to chloride attack, there is a need to develop a testing methodology which can be used to monitor the deterioration process through both the initiation and propagation phases [19]. Given that chloride ingress and chloride induced corrosion in reinforced concrete are influenced by the properties of cover-zone concrete, several attempts have been made to monitor the performance of this region despite still being limited in scope [20, 21]. There is now increasing attention by the international community directed towards the application of the electrical properties of concrete as a candidate durability index in assessing concrete performance [14–17, 22–25].

The current study focusses on monitoring the response of concrete cover-zone subjected to a simulated chloride environment employing an intermittent wetting/drying regime over a period of ~400 days; the condition of the steel surface was also investigated thereby evaluating both the initiation and propagation components of service life in parallel. Discretized electrical resistance/resistivity measurements were undertaken within the cover-zone and a *normalisation* method was developed to study the effect of chloride ingress on the electrical properties of the concrete. Electrical resistivity (or its reciprocal conductivity) of concrete is strongly linked to the microstructure of the cementitious binder, the connected porosity and conductivity of the pore-solution contained within the capillary pore network [14-17]. Resistivity thus represents an important parameter in evaluation of the quality of the concrete; furthermore, in the region of corrosion activity, the corrosion current will pass in part through

103 the steel and in part through the concrete, hence the electrical properties of the concrete
104 surrounding the rebar will play an important role in corrosion dynamics.

105 Macro-cell current and half-cell potential measurements were used to study the condition of
106 the steel surface and identify when depassivation occurs. At the end of the testing programme,
107 dust drillings were taken to establish the chloride concentration profile through the cover-zone
108 and, in addition, the steel reinforcement was retrieved from the concrete for gravimetric (mass
109 loss) corrosion measurements.

110 **2. Experimental Programme**

111 *2.1. Materials and Samples*

112 The concrete mixes used within the experimental programme are presented in Table 1; the 28-
113 day compressive strength of the concretes is also presented in Table 1. The cementitious
114 binders comprised Portland cement (PC) clinker, CEM I 52.5N to EN197-1 [26]; CEM I
115 cement blended with low-lime fly-ash (FA) to EN450-1 [27] and CEM I cement blended with
116 ground granulated blast-furnace slag (GGBS) to EN15167-1 [28]. The chemical composition
117 of the binders used in this study is presented in Table 2. A crushed granite coarse aggregate
118 (conforming to 4/20 grading [29]) and matching fine aggregate (conforming to 0/4 grading [29])
119 were used throughout; additional properties are given in Table 3. For w/b = 0.4, a mid-range,
120 water reducer/plasticizer (SikaPlast 15RM) conforming to BS EN 934-2 [30] was used to
121 ensure adequate workability. The workability (slump) of concrete mixes was classified as S3
122 as specified in BS 8500-1 [31]; the slump test results are presented in Table 1. The mixes in
123 Table 1 are such that, when considered in terms of binder content, binder composition and
124 strength class, mixes with w/b = 0.4 would satisfy the requirements specified in BS 8500-1 [31]
125 to resist environmental exposure classes XD (corrosion induced by chlorides other than from
126 sea water) and XS (corrosion induced by chlorides from sea water) for the majority of the cover

127 thicknesses (>35mm) and an intended working life of at least 100 years. The mixes with w/b =
128 0.6 were chosen to represent poor practice and result in corrosion initiation within the confines
129 of the experimental programme.

Mix	w/b	Water (kg/m^3)	CEM I (kg/m^3)	GGBS (kg/m^3)	FA (kg/m^3)	Coarse (kg/m^3)	Fine (kg/m^3)	Plast (kg/m^3)	Slump (mm)	F_{28} (MPa)
CEM I (PC)	0.4	184	460	0	0	1012	650	1.84	140	64.9
	0.6	180	300	0	0	1101	707	0	110	38.4
CEM III/A (40% GGBS)	0.4	180	450	180	0	1016	652	1.35	100	53.9
	0.6	180	300	120	0	1096	704	0	110	45.6
CEM II/B-V (30% FA)	0.4	212	530	0	160	890	571	1.59	130	49.0
	0.6	180	300	0	90	1078	692	0	100	24.1

Note: w/b = water/binder ratio; Coarse = 4/20 coarse aggregate; Fine = 0/4 fine aggregate; Plast=Plasticizer

Table 1. Concrete mixes used in experimental programme

% by weight	SiO_2	Al_2O_3	Fe_2O_3	CaO	MgO	TiO_2	P_2O_5	SO_3	K_2O	Na_2O	Fineness (% retained on 45μm)
CEM I (PC)	20.68	4.83	3.17	63.95	2.53	+	+	2.80	0.54	0.08	+
FA	51.00	27.40	4.60	3.40	1.40	1.60	0.30	0.70	1.00	0.20	< 29.8
GGBS	33.27	13.38	0.56	41.21	8.49	0.9	+	0.62	0.5	0.33	< 7.8

Table 2. Oxide analysis of binders (+ = not determined)

Aggregate Type	Absorption (%)	Bulk density (kg/m^3)	Specific gravity	Fineness Modulus	Aggregate Impact Value (%)
Coarse	1.02	1450	2.63	6.04	8.2
Fine	2.0	1520	2.63	2.89	+

Table 3. Properties of Coarse and Fine Aggregates

Concrete slabs were mixed using a concrete pan mixer (0.1m^3 capacity) in accordance with BS 1881-125 [32]. With reference to Fig. 1, the concrete slabs (250×250×170mm) were fabricated using a plywood mould which had been given a coat of proprietary release agent (Sika Release Mould Formwork Release Agent) prior to casting. To allow ponding of the concrete surface, an 18-mm dyke was cast into each slab. During casting, the moulds were filled in two layers with each layer compacted using a vibrating table. Three slabs were cast for electrical resistance measurements and macro-cell/half-cell potential measurements (Fig. 1). Each slab contained the following:

(i) four mild steel bars (Ø16×350mm) comprising two working electrodes and two counter electrodes (see Fig. 1(a));

(ii) four pairs of stainless-steel pin electrodes (316L marine grade; Ø2.4×110mm) which were mounted parallel to the steel bars and positioned at 5, 15, 25 and 35mm from the exposed surface. A further four electrodes were positioned in a co-linear or Wenner [33] arrangement at a depth of 70mm from the exposed surface (see Fig. 1(b));

(iii) two sets of co-linear electrodes, also in a Wenner arrangement, mounted at right angles to the mild steel bars and positioned at 25mm (see Fig. 1(c)) and 70mm from the exposed surface (see Fig. 1(d)). The tips of the electrodes located at 25mm were positioned on the heat-shrink sleeving as shown in Fig. 1(c); and,

(iv) one thermistor positioned at 25mm from exposure surface to obtain the temperature of the concrete (see Fig. 1(c)).

An additional slab was cast without any embedded steel bars or electrodes which used to obtain chloride concentration versus depth profiles at the end of the experimental programme.

Prior to casting, all mild-steel bars were cleaned and degreased with acetone and then weighed. Heat shrinkage sleeving was used to form two different exposure areas

(a) the two counter electrodes (see Fig. 1(c) and (d)) had 150mm of steel exposed (75.4cm^2); and,

(b) two working electrodes – one with 150mm of steel exposed a working area of 30.16cm^2 (see Fig. 1(d)) and one comprising two, 50mm exposed areas of steel giving a working area of 2×25.14 cm^2(see Fig. 1(c)).

Regarding the working electrodes, the steel bar with larger exposure area is denoted L_{exp} and the bar with the smaller exposure area denoted by S_{exp}. The working electrode was connected electrically to the counter electrode positioned immediately below it.

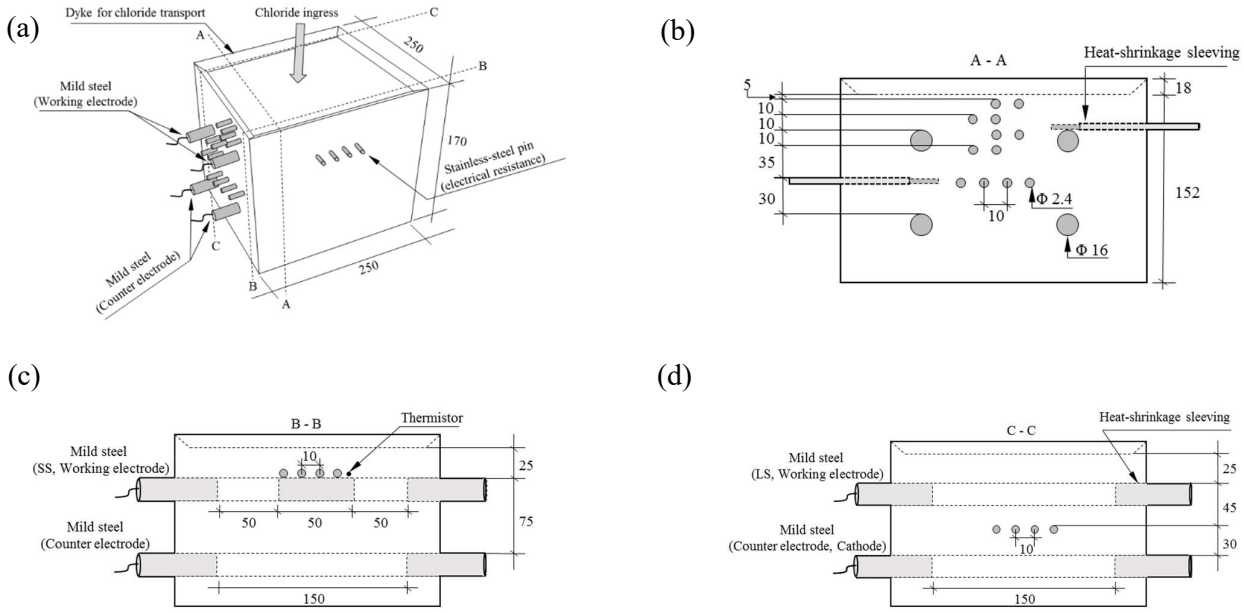

Fig. 1 Showing positioning of electrodes, steel bars and thermistor within concrete slabs, (a) overall schematic, (b) section on A-A, (c) section on B-B and (d) section on C-C.

All the stainless-steel pin electrodes were sheathed with heat-shrink sleeving to expose a 20mm tip. Each electrode-pair had a 10mm centre-to-centre (c/c) spacing. The Wenner co-linear electrode arrangements also had 10mm c/c spacing. As the electrical field between the

168 electrode-pairs is non-uniform, they had to be calibrated to enable resistance measurements (in
169 ohms) to be converted to resistivity (in ohm-m). This was achieved using the Wenner electrode
170 array at 70mm and positioned at the centre of each slab. With this arrangement, the slab can be
171 regarded as an infinite medium [34] and the resistivity of the concrete, ρ_{conc}, is given by,

172 $$\rho_{conc} = 4\pi a R_{Wenner}\ (\Omega m) \quad (1)$$

173 where a is the spacing between the electrodes (=0.01m) and R_{Wenner} is the measured resistance
174 in the Wenner arrangement. The four electrodes on the Wenner array can also be coupled to
175 give three, two-electrode pairings with a 10mm c/c spacing (i.e. the same arrangement as the
176 electrodes within the surface 35mm); if the resistance measured using an electrode-pair is
177 denoted, $R_{el\text{-}p}$, then,

178 $$\rho_{conc} = kR_{el-p}\ (\Omega m) \quad (2)$$

179 where k is the calibration factor for the two-electrode geometry. This was undertaken for all
180 slabs (after 42-days curing) and the calibration curve is presented in Fig. 2, with the slope of
181 the linear-fit curve representing the geometrical constant, k, in equation (2). The error bars
182 represent ± 1 standard deviation about the mean value; where error bars appear to be missing
183 the data marker is larger than the error bar. From Fig. 2, the calibration factor, k, for the
184 electrode-pairs was evaluated as 0.0256m.

185 After casting, all slabs were tightly wrapped with polythene sheeting and placed in a
186 temperature controlled room (20 ± 3ºC, 50 ± 2% RH) for 7-days before demoulding. In order
187 to simulate the one-dimensional (1-D) case, on de-moulding, all surfaces of the slab were
188 double-coated with a high-build epoxy-resin paint, except for the working surface (i.e. the
189 surface with the ponding dyke). The slabs were again wrapped with polythene and cured for a
190 further 28-days in the temperature-controlled room. In this study, an intermittent wetting and
191 drying regime was chosen which is more realistic for simulating chloride ingress (e.g. highway

192 structures [31]), compared to other methods such as pre-mixed chlorides. Prior to the
193 intermittent wet/dry regime, slabs were saturated with distilled water for 7-days to avoid rapid
194 ingress of chloride into slabs after 35-days curing.

195

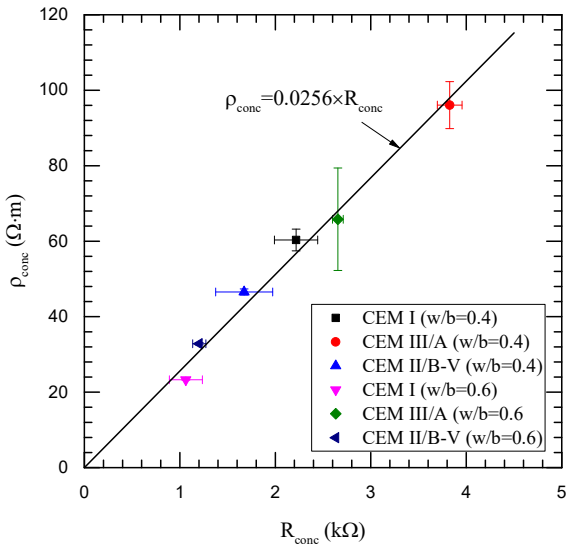

196

197 **Fig. 2** Calibration factor for the two-pin electrode configuration used in this study (error bars
198 represent ± 1 standard deviation).

199 At 42 days, a 0.55 Molar (3.2%) NaCl solution (19.6g/l Cl^-) was ponded on the *dyked* surface
200 of the slab. This chloride concentration is typical of the North Sea [35]. The solution was
201 removed for the drying phase and the surface of the slab exposed to a temperature-controlled
202 environment (20±3ºC, 50±2% RH). In this study, the intermittent wetting/drying regime
203 adopted was: 2 days drying followed by 5 days wetting for the first month; 5 days drying and
204 2 days wetting for the second month and 8 days drying and 6 days wetting for the remaining
205 period up to ~400 days. The reason for adopting this regime was not to have *artificially* long
206 drying periods yet wishing to induce corrosion within a reasonable time-frame.

207

208 *2.3 Electrical Measurements and Chloride Profiling*

209 Electrical resistance measurements were taken using an Agilent LCR meter (4263B) connected
210 in both two-point (for measurements on electrode–pairs) and four-point modes (for
211 measurements on the Wenner electrode arrays). The electrical resistance was measured with a
212 signal amplitude of 350mV at 1kHz which minimised electrode polarisation effects [36].
213 Electrical resistances were measured at the end of each drying and wetting phase up to the end
214 of the test period (382 days).

215 Chloride profiling was performed at ~390 days to estimate diffusion coefficient and surface
216 chloride concentration using error function solution to Fick's 2nd law viz.,

217 $$C(x,t) = C_s\left(1 - erf\left(\frac{x}{2\sqrt{D_{eff}\cdot t}}\right)\right) \quad (3)$$

218 where $C(x,t)$ is the total chloride concentration (%) at depth of x (m) from the surface after
219 exposure time, t (sec), C_s is the surface chloride concentration (%), D_{eff} is the effective
220 diffusion coefficient (m^2/s). The pre-existing chloride concentration in the concrete mixes was
221 negligible.

222 In this procedure, a 100×250×170mm slice was dry-cut from centre of the plain slab using a
223 diamond concrete saw. Powdered samples were then obtained by drilling laterally into the slice
224 using a 4mm drill bit as shown in Fig. 3. In order to be representative of the bulk concrete
225 powder, multiple drillings (between 6 and 8 at each depth increment) were made to 30mm
226 depth (i.e. > maximum aggregate size). After sieving using a 125μm sieve, at least 10g of
227 powder was collected at each depth increment. The depth of investigation was 0-32mm using
228 a 4mm depth increment for all slabs and 0-64 mm using an 8mm depth increment for CEM I
229 slab (w/b = 0.6) as this slab was contaminated by chloride to a greater depth. The total (acid
230 soluble) chloride concentration was obtained using Chloride QuanTab® strips (manufactured

231 by HACH). After weighing the powder (± 0.001g), it was dissolved in a dilute nitric acid
232 solution (~2 Molar HNO_3) at 80±2ºC for 5 minutes. The suspension was then neutralised with
233 NaOH and the measured chloride concentration (in ppm) was converted into chloride
234 concentration by weight of cement.

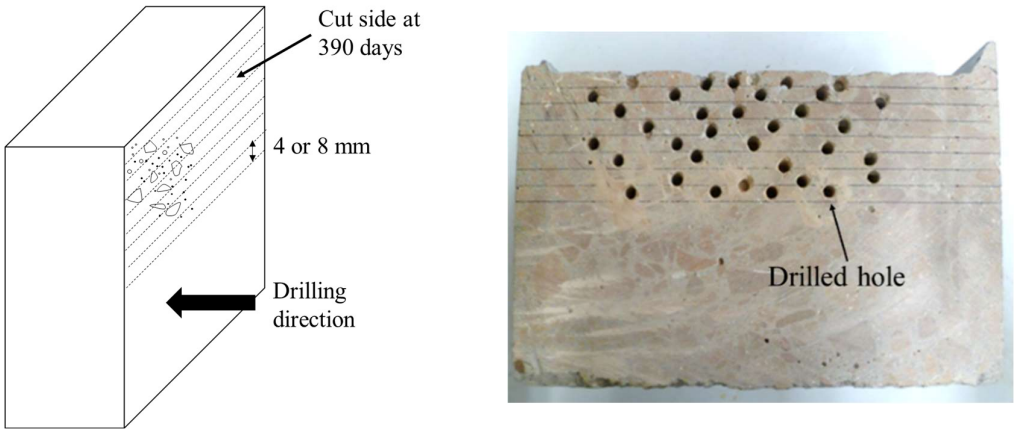

235 **Fig. 3** Drilling procedure for concrete powder collection.

236

237 *2.3. Corrosion tests*

238 To detect chloride-induced corrosion of steel, macro-cell current and half-cell potential
239 measurements were carried out. For macro-cell current measurement, the potential drop across
240 a resistor (R = 1kΩ) between the steel bars at 25mm and 100mm cover depth were measured
241 with a high impedance multi-meter (1705 True RMS programmable multi-meter) at the end of
242 each wet/dry phase. The measurements were conducted after 5-minutes connection to avoid
243 any sudden potential drop. The macro-cell current was then calculated using Ohm's Law and
244 considering only the unsleeved portion of the mild-steel bar as the exposed steel area, viz.,

245 $$i_m = \frac{\Delta V}{R \times A_{exp}} \quad (4)$$

246 where i_m is the macrocell current density (A/m^2), ΔV is the potential drop between two steels
247 (V), R is the resistor (1kΩ), and A_{exp} is the exposure area of steel (m^2).

248 The half-cell potential measurement was undertaken using a copper-copper sulphate reference
249 electrode (CSE) placed on the surface of slabs. The potential drop between the mild-steel bar
250 and the reference electrode was measured using the high impedance multi-meter. The
251 probability of corrosion was then determined using the specification in ASTM C876 [5] and
252 presented in Table 4.

Potential (mV vs CSE)	Potential (mV vs Calomel electrode)	Probability of corrosion
>-200	>-126	Low (<10 %)
-200 to -350	-126 to -276	Intermediate
<-350	<-276	High (>90 %)

253 **Table 4.** Probability of corrosion from potential measurements [5]

254 The mass-loss of the corroded steel bars was used to calculate corrosion rate. In this study,
255 corrosion of steel was only detected in CEM I slabs (w/b = 0.6). After 382 days, the steel bars
256 were retrieved from the slabs and then immersed in 500ml of 60% hydrochloric acid for 20
257 minutes. The steel bars were then cleaned with distilled water. The mass of the cleaned steel
258 bars was measured after approximately 1 hour of drying using a scale of ±0.01g accuracy. The
259 mass loss was calculated with the steel weights before casting and after being cleaned. To
260 compensate mass loss during the mass loss test procedure, three non-corroded steel bars were
261 also applied to the test; thereby the averaged-background loss was determined. From the mass
262 loss data, the average corrosion rate was calculated using Faraday's law,

263 $$i_{corr} = \frac{m_L zF}{tMA_{exp}} \times 1000 \quad (5)$$

264 where i_{corr} is the average corrosion rate (mA/m^2), m_L is the mass loss of corroded steel caused
265 by corrosion products (g), z is the number of electrons transferred in the corrosion process ($=$
266 $2:\ Fe \rightarrow Fe^{2+} + 2e^-$), F is Faraday's constant (= 96,486.7C), t is the duration of the test (s),

267 M is the equivalent mass of material ($Fe = 55.85\ g$), and A_{exp} is the exposure area of steel
268 contributing to the corrosion process (m^2).

269 **3. Result and Discussion**

270 *3.1 Chloride profiling*

271 A knowledge of the chloride distribution within reinforced concrete exposed to chloride-rich
272 environments is essential in order to estimate its residual service life. From the chloride
273 concentration versus depth profile, the effective (or *time-averaged*) diffusion coefficient (D_{eff})
274 and surface chloride concentration, C_s, can be evaluated using equation (3). The concentration
275 is generally expressed as the total chloride content (acid soluble) by % weight of cement [37]
276 as bound chlorides can also participate in corrosion process by reducing the pH of pore solution
277 in concrete [30].

278 Fig. 4 shows the chloride profiles obtained from all concrete slabs at w/b = 0.4 and 0.6 at 390
279 days; D_{eff} and C_s obtained from equation (3) are presented on these Figures. Both CEM II/B-V
280 (w/b = 0.4/0.6) and CEM III/A (w/b = 0.6) exhibit a larger spread in response and could be
281 attributed to the influence of the cyclic wet/dry regime and a wash-out effect [38, 39]. As
282 anticipated, concrete with w/b = 0.6 had higher chloride concentrations at all depths with
283 chlorides penetrating deeper into the slabs in comparison to the w/b = 0.4 slabs. The CEM I
284 concrete was the most vulnerable regarding chloride ingress and the advantage of SCMs in
285 reducing the diffusivity of the concrete is clearly evident. In addition, the intermittent wet/dry
286 regime used in this study would result in a rapid ingress of chloride in concretes with a high
287 w/b ratio (=0.6) due to absorption where the region of the concrete cover-zone most influenced
288 by wet/dry cycles (i.e. the convective zone) would be expected to be greater than those
289 concretes with the low w/b (=0.4).

290

Interestingly, there is a high chloride concentration over the surface ~10mm of concretes containing SCMs (w/b = 0.4) which could result from their high chloride binding capacity [40] and tortuous and disconnected pore network. The chloride concentrations at steel depth (25mm) for concretes with w/b = 0.6 were obtained as 3.4% for CEM I concrete, 0.8% for CEM III/A concrete and 1.04% for CEM II/B-V concrete; all concretes with w/b = 0.4 had low chloride concentrations at steel depth (typically < 0.4% by weight of binder). Although 0.4% of total chloride concentration is considered as an acceptable chloride threshold level (CTL) [18], chloride-induced corrosion of the steel only occurred in CEM I concretes (w/b = 0.6). However, it must be stressed that the CTL for chloride induced corrosion is still controversial [41].

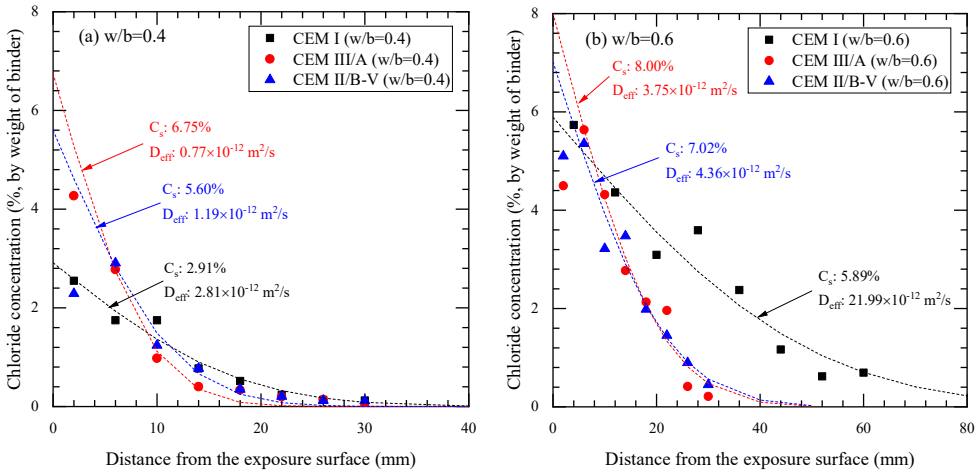

Fig. 4 Chloride profiles for concrete slabs (a) w/b = 0.4, and (b) w/b = 0.6. D_{eff} = effective diffusion coefficient and C_s = surface chloride concentration.

3.2 Electrical resistivity profiles within concrete slabs

As way of illustration, Fig. 5 shows the variation in resistivity for a CEM I concrete (w/b = 0.4) at different depths over the duration of the test period. There are marginal differences in the resistivity obtained from two-pin electrodes at 25mm evaluated using equation (2) and that obtained from the four-pin electrode arrays (Fig. 5(b)) at 25mm and evaluated from equation (1). At 382 days, the resistivity at 25mm from the two-pin electrodes was approximately 17%

lower than that obtained from the four-pin arrangement. This could be attributable to the random distribution of aggregate around the tips of the electrodes.

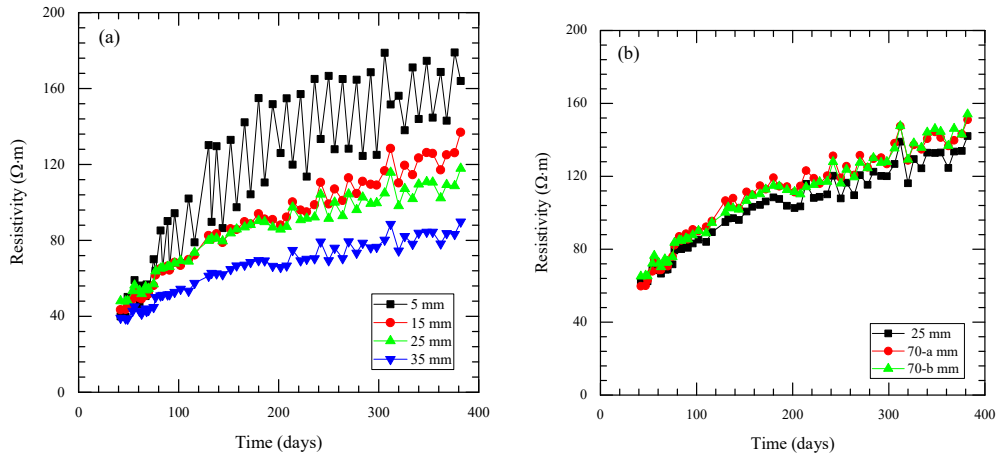

Fig. 5 Change in electrical resistivity at different locations from the concrete surface within CEM I concrete slab (w/b=0.4) using, (a) two-pin electrodes, and (b) four-pin electrode arrays.

Regarding exposure to the natural environment, the main factors which can influence the resistivity are temperature and wetting/drying. The thermistor embedded within each slab at a depth of 25mm was used to monitor temperature changes and Fig. 6 presents the temperature variation in the concrete slabs placed in the laboratory. In Fig. 6, the temperature from all the slabs was averaged with error bars representing ± one standard deviation. The effect of temperature on the resistivity is minimal under laboratory conditions, but could be significant in concrete exposed to the natural environment where the fluctuation of temperature would be considerably greater. In this study, equation (7) was used to *correct* the resistivity to a predefined reference temperature (in this instance, 20°C),

$$\rho_c = \rho_m\left[1 + \alpha(T_m - T_{ref})\right] \quad (7)$$

where ρ_c is the corrected resistivity, ρ_m is the measured resistivity, T_m is the measured temperature, T_{ref} is the reference temperature (20ºC) and α is the temperature coefficient of resistivity with a value of 0.035/ºC [42] used throughout, irrespective of binder type and w/b.

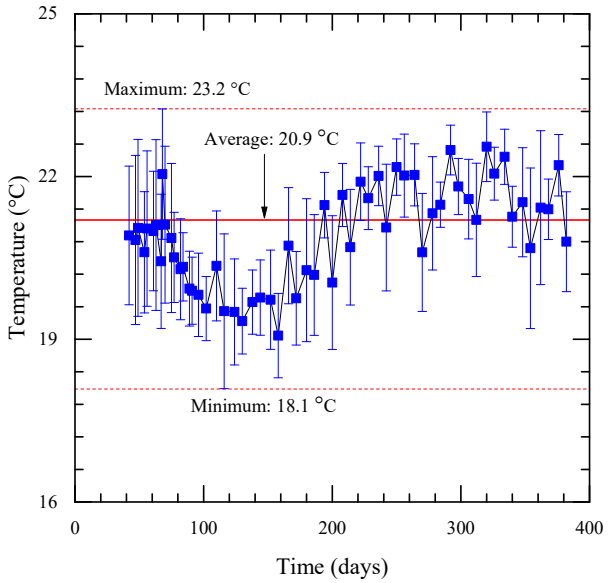

Fig. 6 Temperature variation in concrete slabs stored in the laboratory environment.

Although the temperature changes within the slabs were small, as way of illustration, Fig 7 presents both the as-measured resistivity (at 25mm) and the resistivity corrected to the reference temperature (20°C). It can be observed that the resistivity trend-line becomes *smoother* after the correction; this procedure was undertaken for all the slabs and the results are presented in Fig. 8. It is obvious that the fluctuations in the resistivity still exist after the temperature correction is performed; however, these fluctuations simply reflect the intermittent wetting (resistivity decreases) and drying (resistivity increases) regime. It can be seen that, in some instances, significant fluctuations in the resistivity could be detected to a depth of 35mm for the CEM I (w/b = 0.6) slabs (see Fig. 8(d)). Fig. 8 also shows that there is continual increase in resistivity with time which reflects on-going hydration and pozzolanic activity within the binder and extends well beyond the curing period. From the results at 382 days, the concrete resistivity at 25mm cover (= steel depth) was, respectively, 122.2/33.1Ωm for CEM I concrete

343 (w/b = 0.4/0.6 respectively); 253.1/262.5Ωm for CEM III/A concrete (w/b = 0.4/0.6), and
344 476.8/333.4Ωm for CEM II/B-V concrete (w/b = 0.4/0.6). As expected, CEM I concrete had
345 the lowest resistivity while CEM II/B-V concrete had the highest.

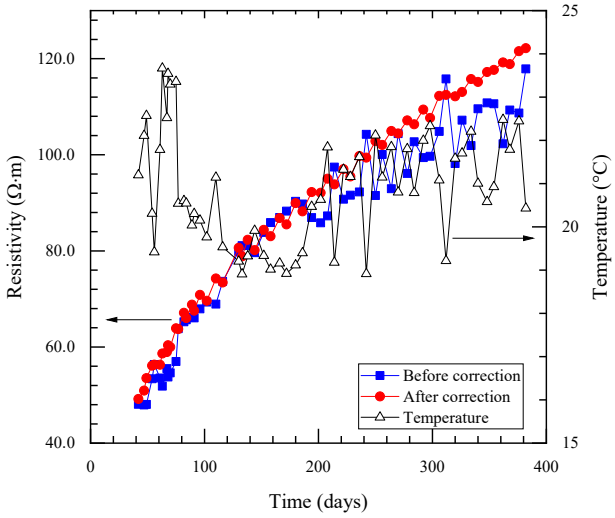

346

347 **Fig. 7** Correction of electrical resistivity (at 25mm) for temperature changes within CEM I
348 concrete, w/b=0.4.

349

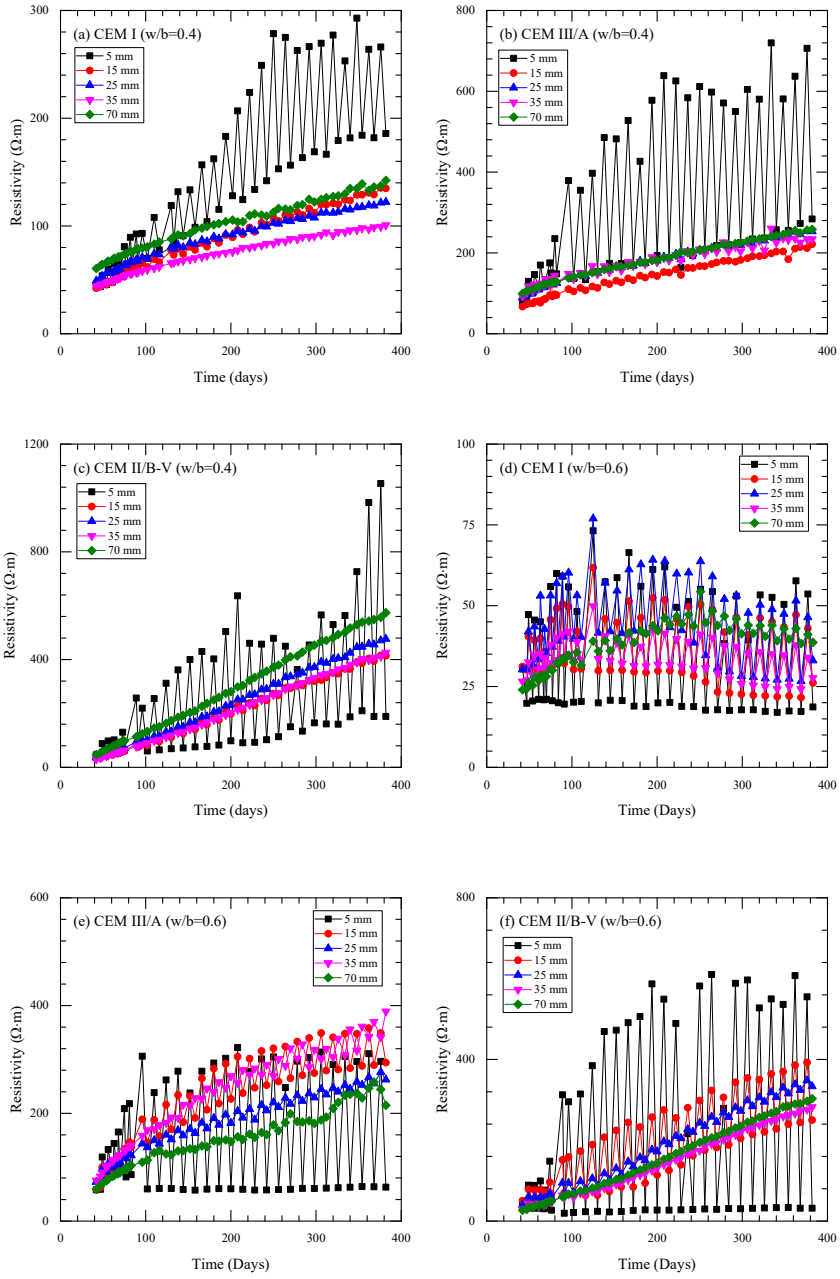

Fig. 8 Electrical resistivity at depths indicated for all mixes after temperature correction.

Empirical resistivity thresholds for inhibition of steel corrosion in reinforced concrete structures has been suggested and these are shown in Table 5 [43]. According to this Table, all concretes, except for CEM I concrete (w/b = 0.6), could be regarded as offering good protection

358 to the steel reinforcement whilst the possibility of corrosion in CEM I concrete (w/b = 0.6)
359 would be very high. With regards to the results of corrosion measurements, these are discussed
360 below.

361

Resistivity (Ωm)	Probable Corrosion Rate
< 50	Very High
50 – 100	High
100 – 200	Moderate / low
> 200	Low

362

363 **Table 5.** Empirical resistivity thresholds for protection of embedded steel reinforcement [43]

364

365 *3.3 Chloride transport and electrical resistance*

366 After correcting for the effect of temperature on the resistivity, Fig. 9 presents the relative
367 increase in resistivity of the concrete (denoted normalised resistivity), $N_{\rho,t}$, at time, t, after the
368 start of the ponding regime where $N_{\rho,t}$ is defined as,

369 $$N_{\rho,t} = \frac{\rho_{c,t}}{\rho_{c,ref}} \quad (8)$$

370 where, $\rho_{c,,t}$ is the measured resistivity of the concrete at time t (Ωm) at a particular electrode-
371 pair and $\rho_{c,ref}$ is the measured resistivity at a reference time at the same electrode-pair, in this
372 case, at the beginning of the intermittent ponding regime (42 days).

373 Fig. 9 shows the normalised resistivity for all mixes which were averaged for the slabs. In this
374 Figure, for clarity, only the results at the end of each wetting phase are presented. Two trends
375 in the resistivity are evident: (i) a continuous increase in resistivity, and (ii) an initial increase

376 in resistivity followed by a decrease. For concretes with high w/b, the decrease in the resistivity
377 would be due to dissolved chlorides entering the capillary pore water. This is particularly the
378 case for the CEM I slabs (w/b = 0.6) (Fig. 9(d)) where a decrease in $N_{\rho,t}$ is detectable over the
379 surface 35mm. On the other hand, the continuous increase in the resistivity at 70mm depth
380 would be due to hydration and pozzolanic reaction as noted above. From the chloride profiles
381 presented in Fig. 4, all concretes were highly contaminated by chloride at 5mm depth even
382 though the resistivity of concretes with low w/b continuously increased with time. This result
383 is similar to the previous studies [44, 45]. Hydration, pozzolanic reaction and chloride binding,
384 which will increase the resistivity, are having a greater effect than the increase in chloride
385 concentration within the pore-water, which would serve to decrease the resistivity, i.e.
386 microstructural changes are having a greater effect than changes in pore-fluid chemistry.
387 Additionally, any increase in ionic concentration within the pore-fluid resulting from an
388 increase in Na^+ and K^+ (and also OH^- for charge balance), would also serve to decrease the
389 bulk resistivity; however, as the same increase in concentration could be expected across the
390 cover depth, it is tacitly assumed that this aspect does not significantly influence the normalised
391 resistivity distribution and hence the results presented in Figure 9.

392

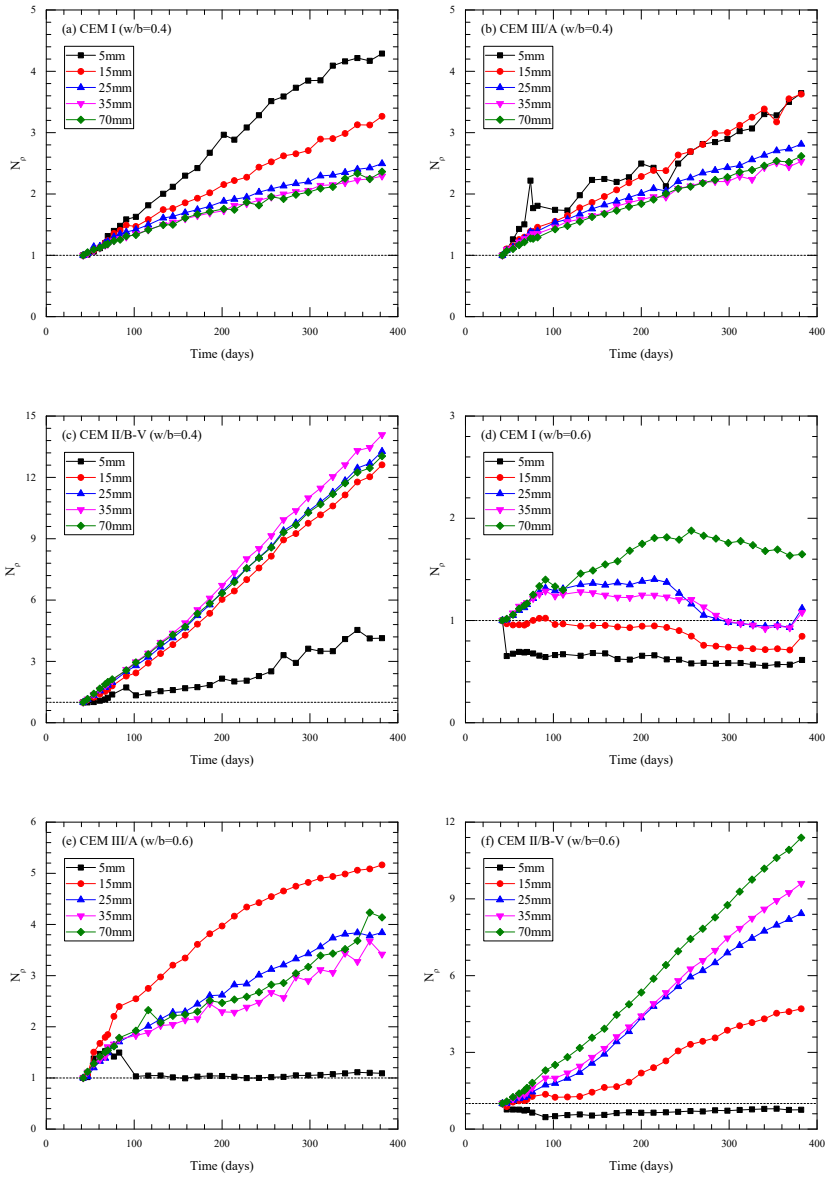

Fig. 9 Normalised resistivity ($N_{\rho,t}$) for all mixes.

The electrical resistivity is dependent on the resistivity of pore solution, porosity, degree of saturation and tortuosity and the contribution of each variable cannot be readily estimated from the measured data. Considering that the concrete at the end of the wetting phase is in a saturated state, resistivity then becomes dependent upon hydration/pozzolanic reaction and free chlorides in the pore water. If it is assumed that hydration is uniform within concrete slab and that

chlorides are negligible at 70mm depth, the effect of chlorides on resistivity could be tracked by considering the *normalised chloride ratio*, N_{Cl}, defined as,

$$N_{Cl} = \frac{N_{\rho,t}}{N_{\rho,t,70}} \quad (9)$$

where $N_{\rho,t}$ is defined in equation (8) above and $N_{\rho,t,70}$ is the normalised resistivity of the concrete at 70mm at the same time.

In Fig. 10, the averaged N_{Cl} is presented for all concretes with time. For concretes with low w/b ratio (w/b = 0.4) at 25mm and 35mm depth, N_{Cl} was distributed around ~1.0 over the test duration. This implies that chloride is having a negligible effect on the resistivity and hydration is main influencing factor. From the chloride profiles in Fig. 4(a), it was also observed that total chloride concentrations at 25mm were <0.2% by weight of binder. On the other hand, it is interesting to note that N_{Cl} was > 1.0 at 5mm for CEM I (Fig. 10(a)) and CEM III/A (Fig. 10(b)) concretes (w/b = 0.4) while the opposite trend was observed for CEM II/B-V (Fig. 10(c)) concrete (w/b = 0.4). Considering only the effect of chloride on the resistivity, an increase in the N_{Cl} indicated densification and refinement of pore structure caused by a chemical or physical reaction between chlorides and the hydration products, whilst N_{Cl} indicates an increase in chloride concentration in the pore solution.

Regarding chloride binding, there are two prominent mechanisms - chemical binding and physical binding. For chemical binding, chlorides react with calcium aluminate hydrates including monosulfate hydrates (AFm) resulting in the formation of Friedel's salt. On the other hand, it has been reported that physical binding is more prominent in cementitious materials than chemical binding [46]; regarding the cement gel, C-S-H is thought to bind chlorides due to its large surface area. From the results for increasing resistance at 5mm cover depth, physical binding could also contribute to a densification of the pore structure. At 5mm cover depth, the

low value of N_{Cl} (<1.0) for CEM II/B-V (w/b = 0.4) could result from a porous structure resulting in a rapid ingress of chloride; however, values of N_{Cl} at the other depths were ~1.0 hence it can be also be concluded that the pore network is more disconnected and tortuous in the CEM II/B-V concrete at depths >5mm.

For concretes with w/b = 0.6, all values decreased relative to 1.0 over the duration of the test program, apart from CEM III/A (w/b = 0.6) (Fig. 10(e)) which only displayed a decrease at 5mm. N_{Cl} decreased initially at all depths and then stabilized; the decrease would be due to the rapid ingress of chloride into the concrete and when N_{Cl} stabilizes an equilibrium appears to be established between chloride ingress and microstructural changes due to hydration and chloride binding. At 15mm and 25mm cover depths for CEM III/A (w/b = 0.6) (Fig. 10(e)), the N_{Cl} values were marginally higher than 1.0 which then decreased at 270 days (15mm) and 354 days (25mm). Again, this would indicate that free chlorides entering the pore water are now having a greater effect than chloride binding and hydration. It has been shown that both w/b and the use of SCMs have a considerable influence of chloride ingress hence the need for a low w/b, partial replacement of the CEM I cement with SCMs and good curing to ensure a long service life. This is now reflected in BS EN 8500-1 [31] as in this code, there is no CEM I concrete specification for XS3 environment (i.e. concrete in the splash and spray zones) for an intended working life of at least 100 years. Considering that only free chlorides initiate corrosion, CEM III/A concrete would be more effective than CEM II/B-V concrete in delaying the corrosion of steel caused by chlorides.

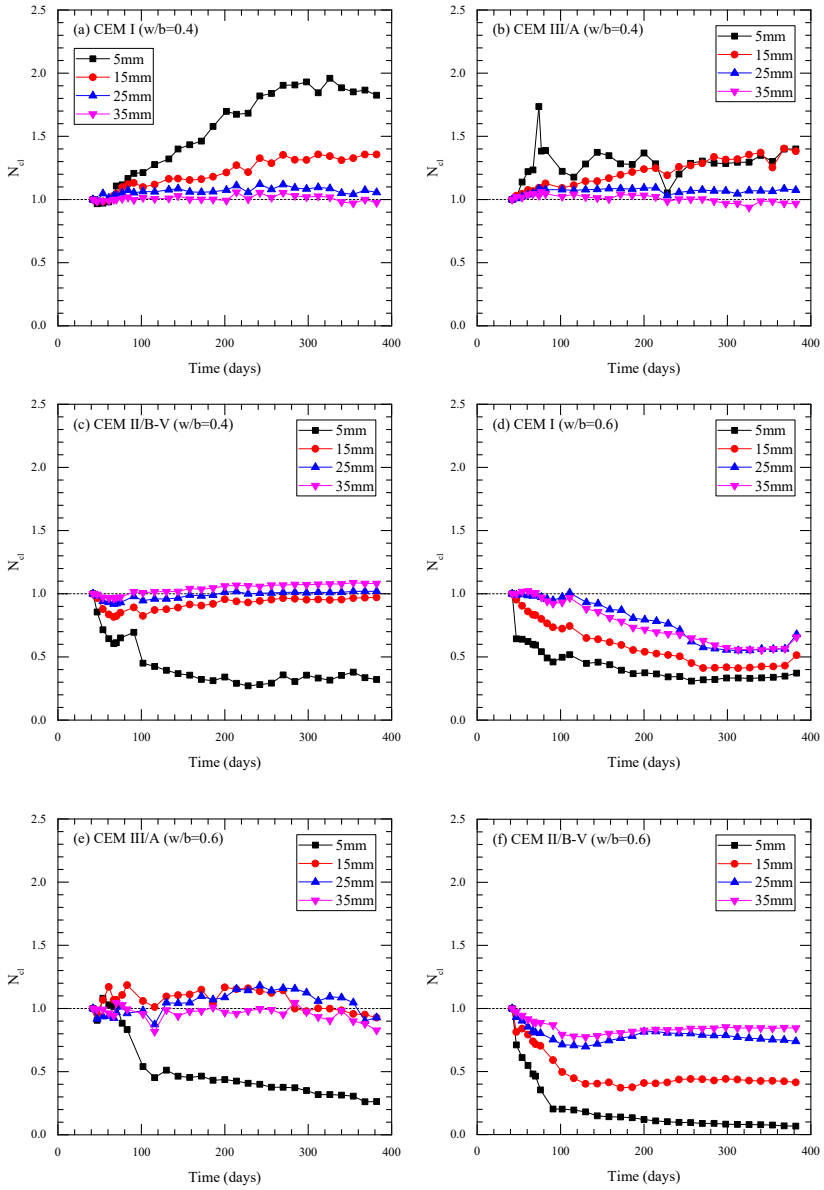

Fig. 10 Normalised resistivity (N_{cl}) for all mixes.

3.4 Chloride-induced corrosion of steel in concrete

Although chlorides trigger depassivation and corrosion, it is still difficult to predict time to corrosion initiation as the chloride threshold level (CTL) is not a single value [41]. To maintain reinforced concrete structures subjected to chloride environments, corrosion monitoring is also required. In this part of the study, macro-cell current and half-cell potential measurements were

carried out to monitor the condition of the steel surface. For clarity, it should be noted that the labelling notation used for the steel-bars is shown in Fig. 11.

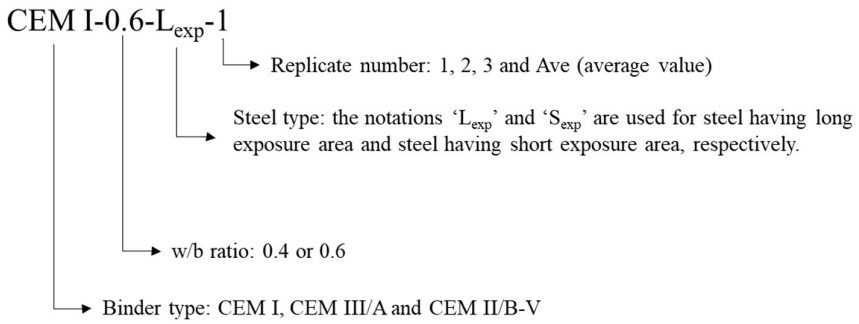

Fig. 11 Steel-bar notation used in the presentation of experimental results

Fig. 12 presents the results regarding averaged corrosion potentials of passivated steel-bars. The boxes represent ± one standard deviation and the whiskers correspond to the maximum and minimum values recorded, respectively. It is apparent that the steel-bars in all concretes, apart from CEM I concrete (w/b = 0.6), were in a passive state during the entire test period. Most corrosion potentials of the steel, irrespective of type of binder and w/b, were > -200mV which indicated a low possibility of corrosion according to ASTM C867 [5]. It was shown that corrosion potentials in concretes with low w/b were more positive compared to concretes with a high w/b which is due to the concrete being more conductive at the high w/b, leading to a lower corrosion potential. Regarding CEM I concrete (w/b = 0.6), after depassivation, there was an apparent change in both macro-cell current and corrosion potential.

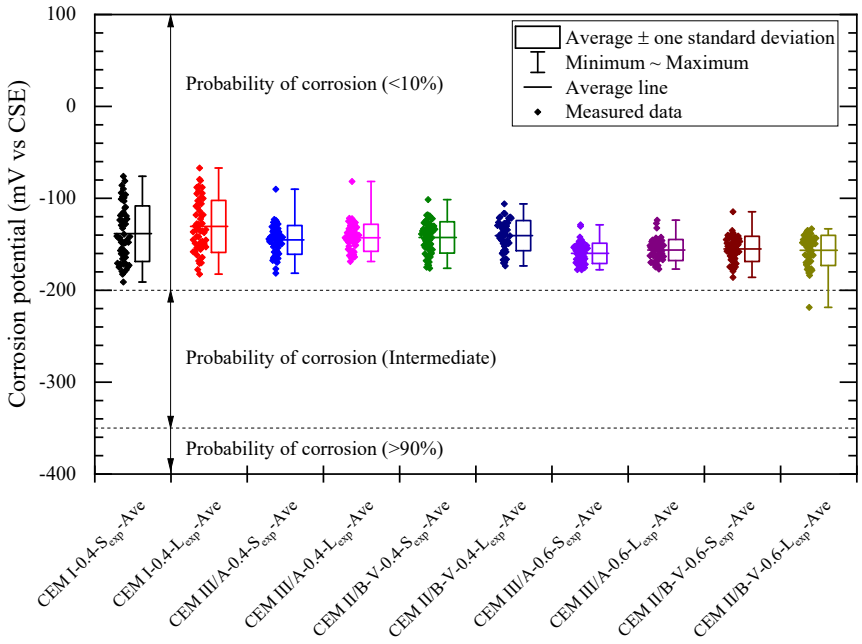

Fig. 12 Corrosion potential of passivated steel for all mixes over the test period (CEM I w/b = 0.6 concrete is presented in Fig. 13).

Fig 13 shows the change from the passive to the active state of steel in CEM I concretes (w/b = 0.6). Once chlorides reached steel level, it was observed that the potential decreased sharply due to an increase in electrical conductivity of pore solution. In passive state, i.e. before reaching -350mV according to ASTM C876, fluctuations of the potential were observed with a wet/dry intermittent regime which suggests that the potential is influenced by exposure conditions as well as condition of steel itself. As expected, after depassivation, the potential decreased rapidly as in previous studies [20, 47, 48] although the time to corrosion initiation varied between 171 days and 317 days, even though the steel-bars were in the same sample or/and the same concrete mix. It can be deduced that initiation of corrosion is affected by various factors including local condition of steel, concrete properties and environmental conditions (oxygen availability, chloride concentration and moisture content) [41]. Considering that a wet/dry intermittent regime was used in this study, a continuous decrease in

corrosion potential could indicate that corrosion process is accelerated due to a sufficient supply of oxygen during the drying phase, although this aspect could also be masked by the reduction in moisture content with increasing wetting/drying cycles. However, as half-cell potential is a qualitative method, it is difficult to evaluate the amount of corrosion products on the steel surface using this measurement [49]

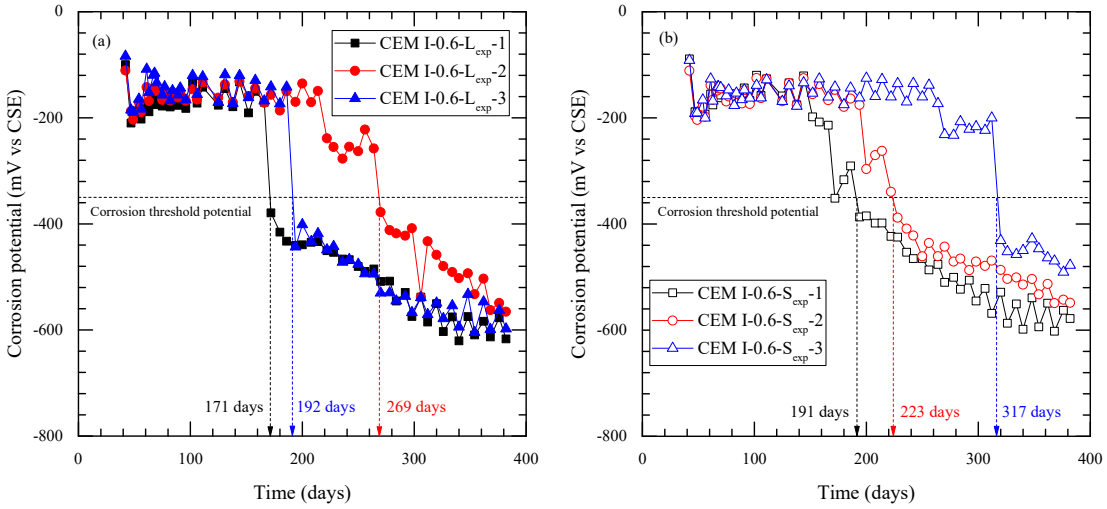

Fig. 13 Corrosion potential of steel bars in CEM I concretes (w/b=0.6) over the test period for (a) steel with long exposure area, L_{exp}, and (b) steel with short exposure area, S_{exp}.

After depassivation, the macro-cell current increases abruptly which is the opposite of the results from the corrosion potential. Although this technique is specified in ASTM G109 as a standard method for detecting corrosion of steel and evaluating severity of steel corrosion in concrete [50], its use is questionable in quantifying the corrosion rate [49]; hence, only the trends in corrosion can be discussed. Macro-cell current, in a similar fashion to corrosion potential, indicates that the steel-bars in all the concretes (apart from CEM I concrete (w/b = 0.6)) were in a passive state during the entire test period. As is evident, from Fig. 14, prior to depassivation, the macro-cell current was stable; in other words, as the same type of steel-bar

504 was used at 25mm and 100mm depth, the current remained ~0mA/m^2 when no corrosion was
505 detected. Some values were lower than 0mA/m^2 (as observed in an earlier study [51]) and could
506 result from the marginal difference in potential between the counter and working electrodes
507 before depassivation, despite the use of the same steel and in the same condition, and the lack
508 of oxygen availability on the steel at 100mm depth due to wetting phase. Fig. 15 shows the
509 changes in macro-cell current after depassivation for CEM I concretes (w/b = 0.6). It can be
510 observed that the current attains values up to ~4mA/m^2 due to a change in the condition of the
511 steel-bar at 25mm cover depth (i.e. the working electrode). It is interesting to observe that the
512 current in CEM I-0.6-L_{exp}-3 decreased significantly after 335 days. The possible explanation
513 is that the counter electrode (i.e. the steel-bar at 100mm depth) was also corroding. However,
514 it is difficult to explain corrosion on the counter electrode below CEM I-0.6-L_{exp}-3 bar as the
515 chloride concentration at 100mm depth from the chloride profiles was negligible and other
516 steels at 100mm depth were in their passive state at that time. From the chloride profiling, as
517 the chloride content at 100 mm depth was low it could be postulated that internal cracking
518 caused by the corrosion products on the steel surface at 25mm leading to more rapid chloride
519 ingress to this depth (and hence the steel counter electrode) as shown in Fig. 16. Time to
520 corrosion initiation is similar to that obtained from corrosion potential and the results presented
521 in Table 6.

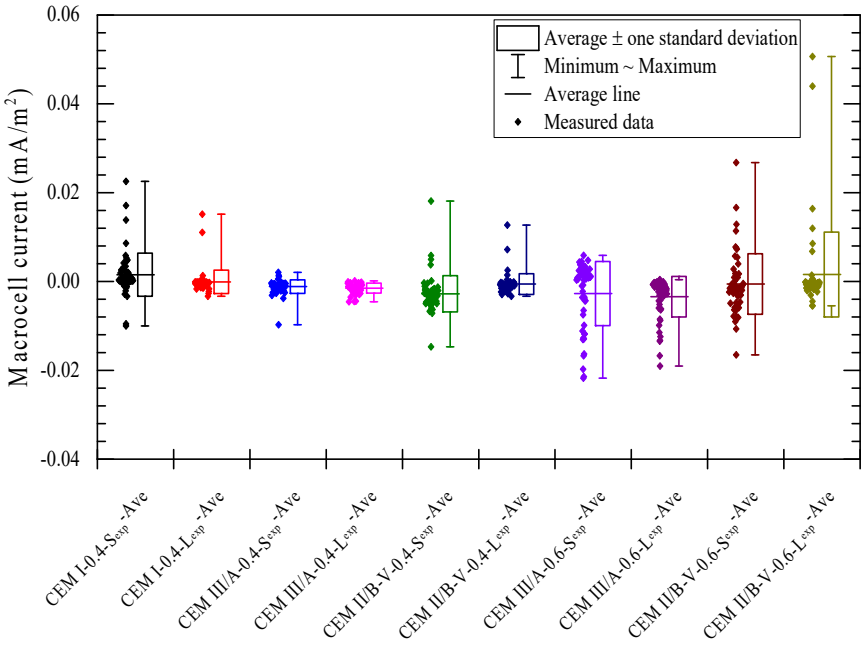

522

523 **Fig. 14** Macrocell current distribution of passivated steel in concrete slabs (Note:
524 CEM I w/b = 0.6 concrete presented in Fig. 15).

525

526

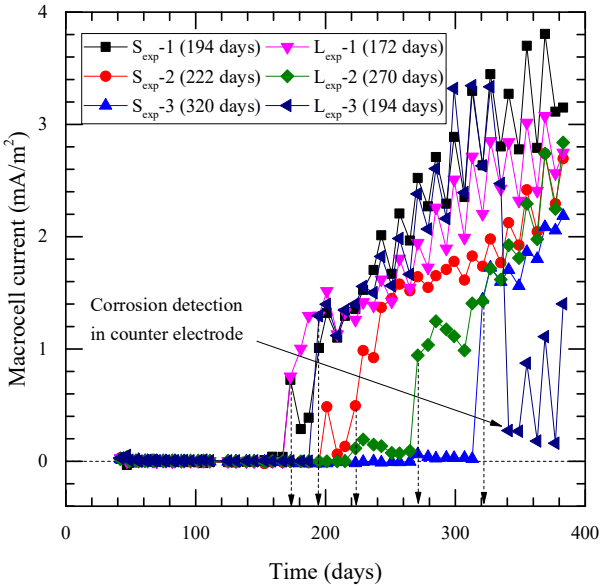

527 **Fig. 15** Macrocell current of steel at 25mm cover-depth in CEM I concrete slabs (w/b=0.6).

528

529

530

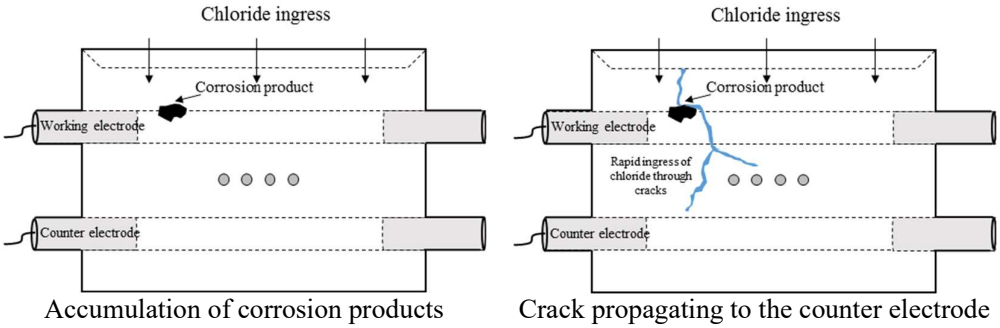

(a)

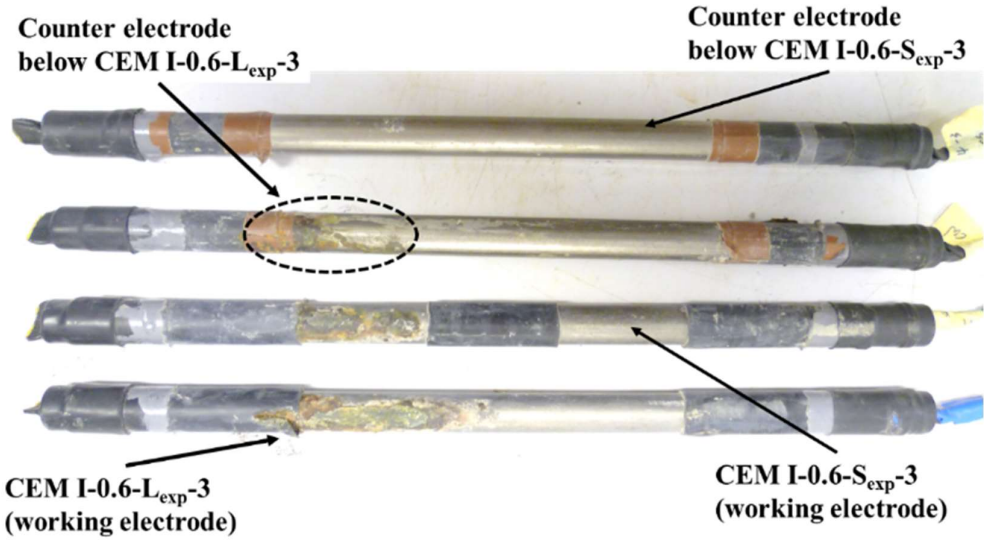

(b)

Fig. 16 Schematic diagrams showing (a) crack pattern caused by chloride-induced corrosion corresponding to CEM I-0.6-L_{exp}-3, and (b) corroded steels (working electrode and counter electrode) in CEM I concrete (w/b=0.6, replicate 3)

Concrete type		CEM I-0.6-					
Steel type		S_{exp}-1	L_{exp}-1	S_{exp}-2	L_{exp}-2	S_{exp}-3	L_{exp}-3
Time to corrosion initiation (days)	Half-cell potential	191	171	223	269	317	192
	Macro-cell current	194	172	222	270	320	194

Table 6. Time to corrosion initiation using two monitoring techniques

3.4 Mass loss and visual inspection for chloride-induced corrosion

Fig. 17 presents the cracking observed on the surface of concrete slabs caused by corrosion of steel which has been highlighted in black. Although the chemical composition of corrosion products was not analysed in this study, the main product that can be deduced is $Fe(OH)_3$ as oxygen is readily available during the intermittent wet/dry regime [43]; in addition, green-rust was also visually observed which is related to chloride attack [52]. After depassivation, it can deduced that the development of cracking is rapid and the propagation of cracking is unpredictable, hence, it is reasonable to decide that the serviceability limit state of reinforced concrete subjected to chloride environments is reached at steel depassivation.

563

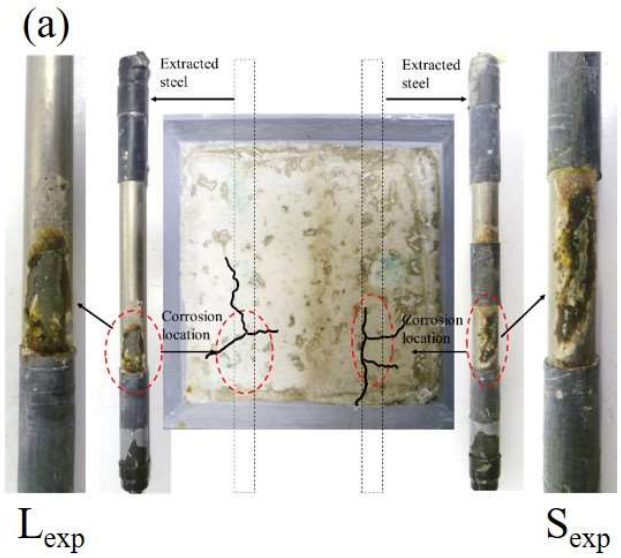
(a)
Extracted steel
Extracted steel
Corrosion location
Corrosion location
L_{exp}
S_{exp}

564

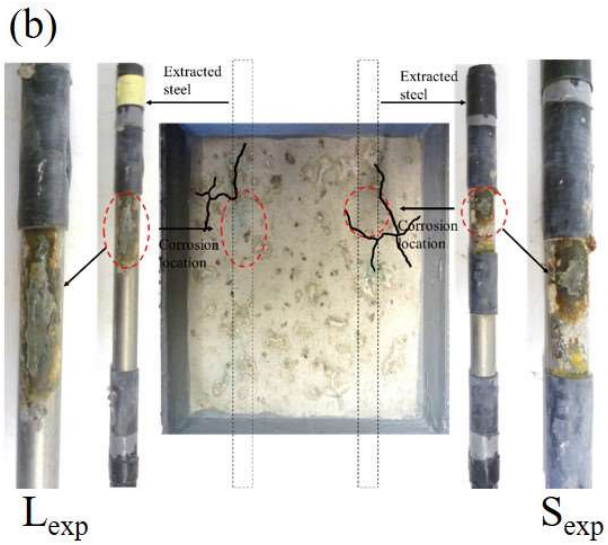
(b)
Extracted steel
Extracted steel
Corrosion location
Corrosion location
L_{exp}
S_{exp}

565

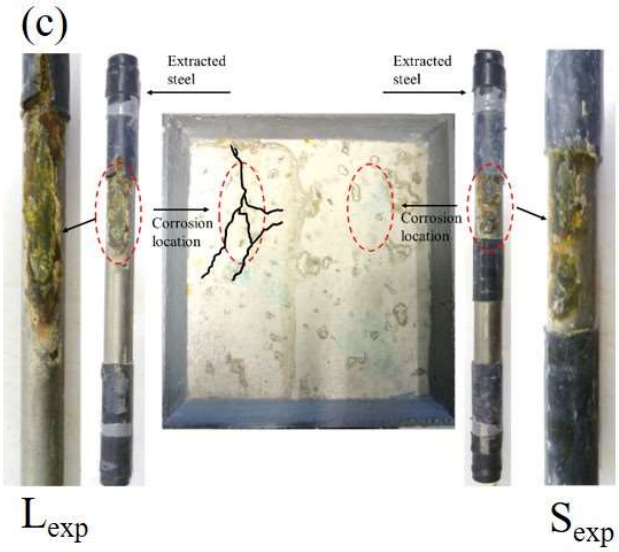

566

567 **Fig. 17** Showing crack patterns on the concrete surface and corrosion on steel extracted from
568 steels for CEM I concretes (w/b=0.6), (a) sample 1, (b) sample 2, and (c) sample 3. Note: L_{exp}
569 on left side and S_{exp} on right side.

570

571 After 382 days, the corroded steels were retrieved from the CEM I concretes (w/b = 0.6) to
572 measure the mass loss. Corrosion rates were estimated using equation (5) and the results are
573 presented in Table 7. Apart from CEM I-0.6-S_{exp}-3, values were, in the main, >10mA/m^2,
574 which corresponds to a high level of corrosion according to RILEM TC 154-EMC [52].
575 Obviously, a wet/dry intermittent regime accelerates corrosion propagation as well as the
576 ingress of chloride; oxygen availability is also increased during drying phase. The corrosion
577 rate obtained from mass loss test is the time-averaged value; thereby corrosion rate at 382 days
578 could be higher than the evaluated values from mass loss test considering that the values during
579 the initial period after depassivation are lower. In addition, although the exact anodic area
580 cannot be estimated, it can be observed that the anodic area is significantly smaller than the
581 exposed area of the steel used in the calculation; hence the real corrosion rate would be

582 considerably higher than the values obtained in this study. In such cases, it has been suggested
583 that a pitting factor should be considered which generally lies in the range 4-10 [2, 54].

Concrete type	CEM I-0.6-					
Steel type	S_{exp}-1	L_{exp}-1	S_{exp}-2	L_{exp}-2	S_{exp}-3	L_{exp}-3
Mass before corrosion (g)	551.23	551.37	551.25	551.22	551.21	551.32
Mass after treatment (g)	550.31	550.40	550.63	550.33	550.94	549.99
Mass loss considering background loss* (g)	0.84	0.89	0.54	0.81	0.19	1.25
i_{corr} (mA/m^2)	17.50	12.36	11.25	11.25	4.00	17.36

* Background loss: 0.08g

584 **Table 7.** Corrosion rate of steel in concrete using mass loss method (CEM I concrete,
585 w/b=0.6))

586

587 **4. Conclusions and Concluding Comments**

588 Discretized electrical resistance/resistivity measurements within the concrete cover-zone were
589 used to investigate chloride due to intermittent wetting/drying of the concrete surface. In
590 parallel with monitoring the resistivity through the cover-zone, chloride profiling, mass loss,
591 half-cell potential and macro-cell current measurements were also undertaken to study the
592 condition of the steel surface and extent of corrosion. From this study, the following
593 conclusions can be drawn.

594 (1) The electrical resistivity of the concrete mixes (apart from CEM I w/b = 0.6) continually
595 increased over the test period indicating that hydration and pozzolanic reaction extended
596 well beyond the initial curing period. Relative to the resistivity of the concrete at the end
597 of the curing period (42-days), the resistivity increased by a factor between 2.5-14, the
598 greatest increase being for the fly-ash concrete (CEM II/B-V). Resistivity measurements

indicated that for concretes with w/b = 0.4, the surface 0-5mm was most influenced by the cyclic wetting/drying regime; however, for concretes with w/b = 0.6, this increased to 0-35mm. This could thus be regarded as the convective zone for the cover region.

(2) Two competing factors influencing resistivity were identified – hydration, pozzolanic reaction and chloride binding which increased the resistivity through microstructural changes, and free chlorides entering the pore water which decreased the resistivity. This was highlighted by expressing the resistivity in terms of the normalised chloride ratio (N_{Cl}). When chlorides in the pore solution started to dominate over microstructural changes, could be detected by a decrease in N_{Cl}.

(3) Using discretized electrical measurements, the resistivity of the concrete in the immediate vicinity of the steel could be measured (i.e. the resistivity at 25mm from the surface). The resistivity of the concrete plays an important role in sustaining corrosion and CEM I (w/b = 0.6) concrete, with the lowest resistivity values at 25mm (~35Ωm), was the only concrete in which corrosion was detected indicating the importance of this parameter in the long-term performance of concrete. Those concretes containing SCMs developed the highest resistivity and no corrosion activity was detected in these slabs.

(4) Macro-cell current and half-cell potential indicated the change in the steel surface from a passive to an active state and could be identified by an abrupt increase or decrease, respectively, in the measured value. However, such techniques are qualitative and provide no information on the rate of corrosion.

(5) Mass-loss measurements provided the corrosion rate whereas visual inspection of the steel indicated localised corrosion on the steel surface. This implies that actual corrosion rates will be considerably higher than those obtained from mass-loss measurements alone. Cracking caused by the products of corrosion was observed, but the behaviour of cracking

623 was unpredictable as some of the cracks extended towards the opposite side of where the
624 corrosion products were formed on the steel.

625 In a broader sense, it has been shown that the measurement of the electrical resistivity at
626 discrete points allows an integrated assessment of both spatial and temporal change in cover-
627 zone performance; it also allows the study of depth-related features which, ultimately, have an
628 important influence on concrete performance, e.g. hydration, the convective zone, water/ionic
629 ingress, concrete resistivity at steel depth.

630

631 **Conflict of Interest**

632 The authors declare that there is no conflict of interest.

633

634 **Acknowledgements**

635 The Authors wish to thank Professor Malcolm Chrisp (Head of School) for placing the facilities
636 of the School at their disposal.

637

638

REFERENCES

[1] A.E.K. Jones, B.K. Marsh, L.A. Clark, B. Seymour, P.A.M. Basheer, A.E. Long (1997) Development of a holistic approach to ensure the durability of new concrete construction. British Cement Association (BCA), BCA Research Report C/21, Camberley, UK, October, 81pp.

[2] K. Tuutti, Corrosion of steel in concrete, PhD Thesis, Lund University, Stockholm, (1982), ISSN 0346-6906. https://lucris.lub.lu.se/ws/files/4709458/3173290.pdf

[3] L. Tang, Chloride transport in concrete - measurement and prediction, PhD Thesis, Chalmers University of Technology, Gothenburg, (1996), ISSN 1104-893X.

[4] K.D. Stanish, R.D. Hooton, Testing the Chloride Penetration Resistance of Concrete : A Literature Review, No. FHWA Contract DTFH61-97-R-00022. United States. Federal Highway Administration, (2001). https://www.fhwa.dot.gov/publications/research/infrastructure/structures/chlconcrete.pdf

[5] ASTM C876 Standard test method for corrosion potentials of uncoated reinforcing steel in concrete, ASTM International, West Conshohocken, PA, (2015).

[6] F. Lollini, E. Redaelli, L. Bertolini, Investigation on the effect of supplementary cementitious materials on the critical chloride threshold of steel in concrete, Mater. Struct. 49 (2016) 4147–4165. https://doi.org/10.1617/s11527-015-0778-0 .

[7] U. Angst, B. Elsener, C.K. Larsen, Ø. Vennesland, Chloride induced reinforcement corrosion: Rate limiting step of early pitting corrosion, Electrochim. Acta. 56 (2011) 5877–5889. https://doi.org/10.1016/j.electacta.2011.04.124 .

660 [8] A.M. Hassanein, G.K. Glass, N.R. Buenfeld, The use of small electrochemical
661 perturbations to assess the corrosion of steel in concrete, NDT E Internatinal. 31 (1998)
662 265–272. https://doi.org/10.1016/S0963-8695(98)00010-3 .

663 [9] O. Anterrieu, B. Giroux, E. Gloaguen, C. Carde, Non-destructive data assimilation as a
664 tool to diagnose corrosion rate in reinforced concrete structures, J. Build. Eng. 23 (2019)
665 193–206. https://doi.org/10.1016/j.jobe.2019.01.033 .

666 [10] NORDTEST, NT BUILD 492: Concrete, mortar and cement-based repair materials:
667 Chloride migration coefficient from non-steady-state migration experiments, (1999).
668 http://www.nordtest.info/images/documents/nt-
669 methods/building/NT%20build%20492_Concrete%20mortar%20and%20cement-
670 based%20repair%20materials_Chloride%20migration%20coefficient%20from%20non
671 -steady-state%20migration%20experiments_Nordtest%20Method.pdf .

672 [11] A.S. El-Dieb, T.A. El-Maaddawy, Assessment of reinforcement corrosion protection of
673 self-curing concrete, J. Build. Eng. 20 (2018) 72–80.
674 https://doi.org/10.1016/j.jobe.2018.07.007 .

675 [12] B. Elsener, J. Gulikers, R. Polder, M. Raupach, Half-cell potential measurements-
676 Potential mapping on reinforced concrete structures, Mater. Struct. 36 (2003) 461–471.
677 https://doi.org/10.1007/BF02481526 .

678 [13] F. Matalkah, T. Salem, P. Soroushian, Acid resistance and corrosion protection potential
679 of concrete prepared with alkali aluminosilicate cement, J. Build. Eng. 20 (2018) 705–
680 711. https://doi.org/10.1016/j.jobe.2018.08.001 .

681 [14] J.G. Kessy, M.G. Alexander, H. Beushausen, Concrete durability standards :
682 International trends and the South African context, J. S. Afr. Inst. Civ. Eng. 57 (2015)
683 47–58. http://dx.doi.org/10.17159/2309-8775/2015/v57n1a5 .

[15] K. Li, Z. Chen, H. Lian, Concepts and requirements of durability design for concrete structures : an extensive review of CCES01, Mater. Struct. 41 (2008) 717–731. https://doi.org/10.1617/s11527-007-9276-3 .

[16] Japan Society of Civil Engineers, Standard specifications for concrete structures – 2007: Design, (2007).

[17] Japan Society of Civil Engineers, Standard specifications for concrete structures-2007: Maintenance, (2007).

[18] British Standards Institution, BS EN 206:2013+A1:2016 Concrete — Specification, performance, production and conformity, (2016).

[19] W.J. McCarter, Ø. Vennesland, Sensor systems for use in reinforced concrete structures, Constr. Build. Mater. 18 (2004) 351–358. https://doi.org/10.1016/j.conbuildmat.2004.03.008 .

[20] U.M. Angst, B. Elsener, C.K. Larsen, Ø. Vennesland, Chloride induced reinforcement corrosion: Electrochemical monitoring of initiation stage and chloride threshold values, Corros. Sci. 53 (2011) 1451–1464. https://doi.org/10.1016/j.corsci.2011.01.025 .

[21] P. Romano, P.S.D. Brito, L. Rodrigues, Monitoring of the degradation of concrete structures in environments containing chloride ions, Constr. Build. Mater. 47 (2013) 827–832. https://doi.org/10.1016/j.conbuildmat.2013.05.042 .

[22] N. Singh, S.P. Singh, Electrical resistivity of self consolidating concretes prepared with reused concrete aggregates and blended cements, J. Build. Eng. 25 (2019) 100780. https://doi.org/10.1016/j.jobe.2019.100780 .

[23] A.S. El-Dieb, M.A. El-Ghareeb, M.A.H. Abdel-Rahman, E.S.A. Nasr, Multifunctional electrically conductive concrete using different fillers, J. Build. Eng. 15 (2018) 61–69. https://doi.org/10.1016/j.jobe.2017.10.012 .

[24] K.A. Riding, J.L. Poole, A.K. Schindler, M.C.G. Juenger, K.J. Folliard, Simplified concrete resistivity and rapid chloride permeability test method, ACI Mater. J. 105 (2008) 390–394. https://doi.org/10.14359/19901 .

[25] W.J. McCarter, B. Suryanto, H.M. Taha, S. Nanukuttan, P.M. Basheer, A testing methodology for performance-based specification, J. Struct. Integrity Maint. 2(2017) 78–88. https://doi.org/10.1080/24705314.2017.1318040 .

[26] British Standards Institution, BS EN 197-1:2011 Cement-Part 1: Composition , specifications and conformity criteria for common cements, (2015).

[27] British Standards Institution, BS EN 450-1:2012 Fly ash for concrete - Part 1: Definition, specifications and conformity critera, (2012).

[28] British Standards Institution, BS EN 15167-1:2006 Ground granulated blast furnace slag for use in concrete , mortar and grout — Part 1: Definations, specifications and conformity criteria, (2006).

[29] British Standards Institution, BS EN 12620:2002+A1:2008 Aggregates for concrete, (2008).

[30] British Standards Institution, BS EN 934-2:2009+A1:2012 Admixtures for Concrete, Mortar and Grout - Admixtures for Concrete, (2012).

[31] British Standards Institution, BS 8500-1:2015+A2:2019 Concrete- Complementary British Standard to BS EN 206-1; Part 1:Method of specifying and guidance for the specifier, (2019).

[32] British Standards Institution, BS 1881-125:2013 Testing concrete — Part 125 : Methods for mixing and sampling fresh concrete in the laboratory, (2013).

730 [33] F. Wenner, A method of measuring earth resistivity, Natl. Bur. Stand. 12 (1915) 469–
731 478. https://doi.org/10.6028/bulletin.282 .

732 [34] W.J. McCarter, G. Starrs, S. Kandasami, R. Jones, M. Chrisp, Electrode configurations
733 for resistivity measurements on concrete, ACI Materials Journal, 106(3) (2009) 258-
734 264. https://doi.org/10.14359/56550 .

735 [35] W.J. McCarter, B.T. Linfoot, T.M. Chrisp, G. Starrs, Performance of concrete in XS1,
736 XS2 and XS3 environments, Mag. Concr. Res. 60 (2008) 261–270.
737 https://doi.org/10.1680/macr.2008.60.4.261 .

738 [36] W.J. McCarter, R. Brousseau, The A.C. response of hardened cement paste, Cem. Concr.
739 Res. 20 (1990) 891–900. https://doi.org/10.1016/0008-8846(90)90051-X .

740 [37] G.K. Glass, N.R. Buenfeld, The presentation of the chloride threshold level for corrosion
741 of steel in concrete, Corros. Sci. 39 (1997) 1001–1013. https://doi.org/10.1016/S0010-
742 938X(97)00009-7 .

743 [38] H.W. Song, C.H. Lee, K.Y. Ann, Factors influencing chloride transport in concrete
744 structures exposed to marine environments, Cem. Concr. Compos. 30 (2008) 113–121.
745 https://doi.org/10.1016/j.cemconcomp.2007.09.005 .

746 [39] L.O. Nilsson, A numerical model for combined diffusion and convection of chloride in
747 non-saturated concrete, in: C. Andrade and J. Kropp (Eds.), Proc. 2nd International
748 RILEM Workshop on Testing and Modelling the Chloride Ingress into Concrete, Paris,
749 France, RILEM Publication SARL. Sept., (2000), 261–275. ISBN 2 912143 22 5.

750 [40] H.W. Song, C.H. Lee, M.S. Jung, K.Y. Ann, Development of chloride binding capacity
751 in cement pastes and influence of the pH of hydration products, Can. J. Civ. Eng. 35
752 (2008) 1427–1434. https://doi.org/10.1139/L08-089 .

753 [41] U. Angst, B. Elsener, C.K. Larsen, Ø. Vennesland, Critical chloride content in reinforced
754 concrete - A review, Cem. Concr. Res. 39 (2009) 1122–1138.
755 https://doi.org/10.1016/j.cemconres.2009.08.006 .

756 [42] W.J. McCarter, T.M. Chrisp, G. Starrs, P.A.M. Basheer, J. Blewett, Field monitoring of
757 electrical conductivity of cover-zone concrete, Cem. Concr. Compos. 27 (2005) 809–
758 817. https://doi.org/10.1016/j.cemconcomp.2005.03.008 .

759 [43] J.P. Broomfield, Corrosion of steel in concrete: Understanding, Investigation and Repair,
760 1st Edition, E&FN Spon, London, 1997. ISBN 0 419 19630 7.

761 [44] D. McPolin, P.A.M. Basheer, A.E. Long, K.T. V Grattan, T. Sun, Obtaining progressive
762 chloride profiles in cementitious materials, Constr. Build. Mater. 19 (2005) 666–673.
763 https://doi.org/10.1016/j.conbuildmat.2005.02.015 .

764 [45] R.B. Polder, W.H.A. Peelen, Characterisation of chloride transport and reinforcement
765 corrosion in concrete under cyclic wetting and drying by electrical resistivity, Cem.
766 Concr. Compos. 24 (2002) 427–435. https://doi.org/10.1016/S0958-9465(01)00074-9 .

767 [46] H. Hirao, K. Yamada, H. Takahashi, H. Zibara, Chloride binding of cement estimated
768 by binding isotherms of hydrates, J. Adv. Concr. Technol. 3 (2005) 77–84.
769 https://doi.org/10.3151/jact.3.77 .

770 [47] K.Y. Ann, T.-S. Kim, J.H. Kim, S.-H. Kim, The resistance of high alumina cement
771 against corrosion of steel in concrete, Constr. Build. Mater. 24 (2010) 1502–1510.
772 https://doi.org/10.1016/j.conbuildmat.2010.01.022 .

773 [48] M. Pour-ghaz, O.B. Isgor, P. Ghods, Quantitative interpretation of Half-Cell potential
774 measurements in concrete structures, J. Mater. Civ. Eng. 21 (2009) 467–475.
775 https://doi.org/10.1061/(ASCE)0899-1561(2009)21:9(467) .

776 [49] J.S. Reou, K.Y. Ann, Electrochemical assessment on the corrosion risk of steel
777 embedment in OPC concrete depending on the corrosion detection techniques, Mater.
778 Chem. Phys. 113 (2009) 78–84. https://doi.org/10.1016/j.matchemphys.2008.07.063 .
779 [50] ASTM G109-07 Standard test method for determining the effects of chemical
780 admixtures on corrosion of embedded steel reinforcement in concrete exposed to
781 chloride environments, ASTM International, West Conshohocken, PA (2013).
782 [51] R. Vedalakshmi, K. Rajagopal, N. Palaniswamy, Longterm corrosion performance of
783 rebar embedded in blended cement concrete under macro cell corrosion condition,
784 Constr. Build. Mater. 22 (2008) 186–199.
785 https://doi.org/10.1016/j.conbuildmat.2006.09.004 .
786 [52] D.A. Koleva, J. Hu, A.L.A. Fraaij, P. Stroeven, N. Boshkov, J.H.W. de Wit, Quantitative
787 characterisation of steel/cement paste interface microstructure and corrosion phenomena
788 in mortars suffering from chloride attack, Corros. Sci. 48 (2006) 4001–4019.
789 https://doi.org/10.1016/j.corsci.2006.03.003 .
790 [53] C. Andrade, C. Alonso, Test methods for on-site corrosion rate measurement of steel
791 reinforcement in concrete by means of the polarization resistance method, Mater. Struct.
792 37 (2004) 623–643. https://doi.org/10.1007/BF02483292 .
793 [54] J.A. González, C. Andrade, C. Alonso, S. Feliu, Comparison of rates of general
794 corrosion and maximum pitting penetration on concrete embedded steel reinforcement,
795 Cem. Concr. Res. 25 (1995) 257–264. https://doi.org/10.1016/0008-8846(95)00006-2 .